

# An RF-ID Reader Using SAW Dispersive Delay Lines For Wideband Synchronisation

T.M. McCoy, P.V. Brennan and R.J. Bullock

Department of Electrical and Electronic Engineering, UCL, Torrington Place, London WC1E 7JE, UK.

Email: {tmccoy, pbrennan, rbullock}@ee.ucl.ac.uk

**Abstract**—RF-ID systems are susceptible to frequency interference from other communication systems particularly when the RF-ID tags transmit on a fixed carrier frequency. The RF-ID systems are less vulnerable to frequency interference when frequency diversity is used by the RF-ID system. This paper proposes an architecture for an RF-ID receiver which allows a number of active RF-ID tags with oscillators of low frequency stability to be accommodated within the same RF-ID cell. The synchronisation technique used by the receiver contains a carrier frequency estimator which has been designed using SAW dispersive delay lines. The carrier frequency estimator uses the spectral properties of the received signal to estimate the carrier frequency. The analytic and simulated performance of the carrier frequency estimator has been examined for two peak search algorithms.

**Index Terms**—RF-ID, communication, receiver, synchronisation, wide bandwidth, tags, frequency stability

## I. INTRODUCTION

An active RF-ID system may use a combination of frequency diversity and pulse repetition interval diversity; the former helps to avoid interference problems and the latter helps to avoid repetitive tag clashes with other tags in the same area. Whilst pulse repetition interval diversity used in classical active RF-ID architectures reduces the likelihood of clashing between tags transmitting on the same carrier frequency, it does not prevent in band frequency interference from other systems operating in band from disturbing the narrow band signal transmitted from the tag to receiver, particularly if the interference is continuous in nature. This form of interference could be prevented from harming the reliability of the RF-ID system by allowing the tags to transmit from burst to burst at carrier frequencies anywhere within a band rather than at a fixed frequency. The size of the band determined by the detection agility of the receiver and the chosen frequency stability of the frequency source within the transmitter. Besides making the RF-ID system less susceptible to frequency interference, oscillators of low frequency stability are less expensive than stable fixed frequency PLL sources and therefore provide a lower cost if the RF-ID tag was embedded for example in a

boarding card in an airport. By adopting this approach the complexity of the system is now referred to the receiver in comparison to the methods adopted with traditional active RF-ID systems.

In the proposed system to be investigated, an active RF-ID tag transmits a BPSK (Binary phase shift keyed) modulated carrier to a receiver. The tag can transmit at carrier frequencies anywhere within a wide band of 30 MHz centred on 5.8 GHz but in principle an arbitrarily-wide band can be accommodated by the receiver. The synchronisation technique in the receiver estimates the carrier frequency using the spectral properties of the received pre-amble in the tag data burst. The carrier frequency estimator used by the synchronisation technique is implemented using SAW dispersive delay lines. Although, nowadays almost all the chirp generators and signal processors are digital, SAW dispersive delay lines are more appropriate for the synchronisation technique used in the RF-ID receiver because these devices can be realized with small size, low cost, wide band coverage, low power consumption and have high reliability. More importantly the complex synchronisation circuits in the receiver can be economized since these devices use an analog correlation process to estimate the Fourier transform of the received signal.

The implementation of an RF-ID reader incorporating frequency diversity is considered in this paper. The paper is divided into three parts. The paper begins with a study of the literature in frequency measurement and acquisition. Section III then introduces the architecture of the receiver and the detailed hardware implementation of the carrier frequency estimator (CFE). The last section then examines the performance of the carrier frequency estimator by analysis and simulation for two peak search algorithms.

## II. FREQUENCY MEASUREMENT AND ACQUISITION

Frequency measurement and acquisition can be examined using the following two areas: detection theory [1] and sinusoidal parameter estimation [2]. The analysis is evaluated under the assumption that the modulated carrier signal at the receiver can be considered to be stationary and the modulation components have sufficient separation as to be detected. An unbiased estimator provides a best estimation of the parameters given the available data observations. Maximum likelihood estimators for single

This paper is based on "An RF-ID Receiver Using SAW Filters For Wideband Synchronisation," by T.M. McCoy, P.V. Brennan and R.J. Bullock, which appeared in the Proceedings of the IEEE International Conference on RFID, March 2007, Grapevine, Texas, USA © 2007 IEEE.

This work was supported by the EU Framework 6 STREP programme., Project no. AST3-CT-2004 502858 OPTAG.

tone and multiple tone parameter estimation from discrete observations are detailed in [2], [3]. Equation (1) shows the maximum likelihood (ML) estimator,  $X_{ML}$ .

$$X_{ML} = \max_f \left| \frac{1}{N} \sum_{n=0}^{N-1} x_n \exp(-j2\pi f n T_s) \right|^2 \quad (1)$$

where:  $x_n$  for  $n = 0, 1, \dots, N - 1$  are the available input samples and  $T_s$  is the sampling time. The index with the maximum amplitude is the chosen frequency.

The Cramer-Rao bound describes the lower bound on the variance of any unbiased estimator. Equation (2) shows the Cramer-Rao bound for the maximum likelihood estimator provided there is a single real sinusoidal signal embedded in white, Gaussian noise, with unknown frequency, unknown amplitude and unknown phase:

$$\sigma_f = \frac{\sqrt{12}}{2\pi T_s \sqrt{N(N^2 - 1) SNR}} \quad (2)$$

where:  $N$  is the number of samples and SNR is the signal to noise power ratio.

Indeed the Cramer-Rao bound accurately describes the frequency error in the ML estimator above a certain signal to noise threshold. Since the maximum likelihood estimator is very similar to a Fourier transform, a possible method for coarse frequency estimation of a single frequency is the FFT. This provides an estimate evenly spread over a set of frequency bins based on the number of samples in the transform. The frequency resolution,  $f_{res}$ , of the FFT is inversely proportional to the data time length,  $T_w$ , as shown in (3). It can also be expressed in terms of the sampling time,  $T_s$ , and the number of samples in the transform,  $N$ , which are taken from the time domain signal.

$$f_{res} = \frac{1}{T_w} = \frac{1}{NT_s} \quad (3)$$

In fact, the FFT estimator can also provide an approximation to the maximum likelihood estimator for multiple frequencies separated by more than  $\frac{4}{NT_s}$  or four bins as derived by [3]. The resolution of the FFT estimator can be improved by adding zeros to the end of the signal. This achieves a longer FFT length without modifying the spectral content of signal. Because the zero-padded signal is longer ( though no new energy has been added ), the resulting FFT provides a better frequency resolution. The resolution also determines the maximum error expected from the estimator which occurs whenever when a tone is located halfway between bins. If the tone frequencies are uniformly distributed in  $\pm \frac{f_{res}}{2}$  then the standard deviation of the frequency estimate from a non-zero padded FFT is

$$\sigma_{coarse} = \frac{1}{2\sqrt{3}NT_s} \quad (4)$$

[4] highlights an improvement in the FFT accuracy by using fine frequency estimation and applying windowing functions to achieve maximum dynamic range in the resolution bin. However an optimum FFT-based frequency acquisition is not be required for this application because

as long as a carrier frequency estimate is estimated within the capture bandwidth of the demodulator and before the end of the pre-amble of the tag data burst, then there is no need to perform fine frequency estimation to overcome truncation from the FFT bins.

Now that frequency measurement has been considered, previous attempts at frequency acquisition must be evaluated prior to incorporating carrier synchronisation into the receiver design. A considerable amount of literature has been published on carrier synchronization in the presence of small frequency offsets. These studies are applied to applications where the frequency offset varies by no more than a few 100 kHz. For instance, [5] highlights a method for coarse frequency acquisition for Nyquist filtered MPSK. The estimation procedure looks for a small frequency offset when a BPSK modulated carrier is downconverted to a low pass filtered baseband signal. The offset in the carrier is estimated from the spectral components in the bandlimited BPSK signal. In another example, [6] examines the use of a DFT-based frequency acquisition algorithm for carrier offsets in mobile satellite receivers. An open loop DFT estimation method along with feed forward frequency estimation algorithm is demonstrated with a capture range  $\Delta F$  of only  $\pm 5$  kHz. These types of systems operate on very small variations in the carrier frequency. A more sophisticated receiver design must be considered for much larger variations in the carrier frequency.

### III. RECEIVER SYSTEM

The architecture shown in Figure 1 uses the spatial and frequency domains to detect and estimate the carrier frequency of a short pre-amble burst from each tag transmission. The tag pre-amble consists of alternate zeros and ones modulated onto the carrier using Binary phase shift keyed (BPSK) modulation. The pre-amble therefore contains harmonics that have frequencies at odd multiples of,  $R/2$  Hz where  $R$  is the data rate. The spectral pair with the largest amplitude are the primary modulation components which are separated by  $R$  Hz. Thus the carrier frequency is estimated by the CFE using the arithmetic mean of the primary modulation indices identified during the duration of the tag pre-amble. The estimated frequency from the carrier frequency estimator (CFE) module is then used to set the frequency of a direct digital synthesiser (DDS). The signal is then down converted to a well-defined intermediate frequency (IF) for demodulation by a Costas loop. The design also contains an AGC the design of which must be carefully considered since it must not affect the sensitivity of the carrier frequency estimator (CFE) which performs a two dimensional search in frequency and amplitude during the duration of the tag pre-amble.

By way of an example consider a tag data burst that is received with a random carrier frequency,  $f_c$  within the detection bandwidth,  $\Delta f_b$ , centred on a convenient first intermediate frequency stage. The tag signal bandwidth,  $\Delta f_s$ , is chosen as 1 MHz which means the random carrier

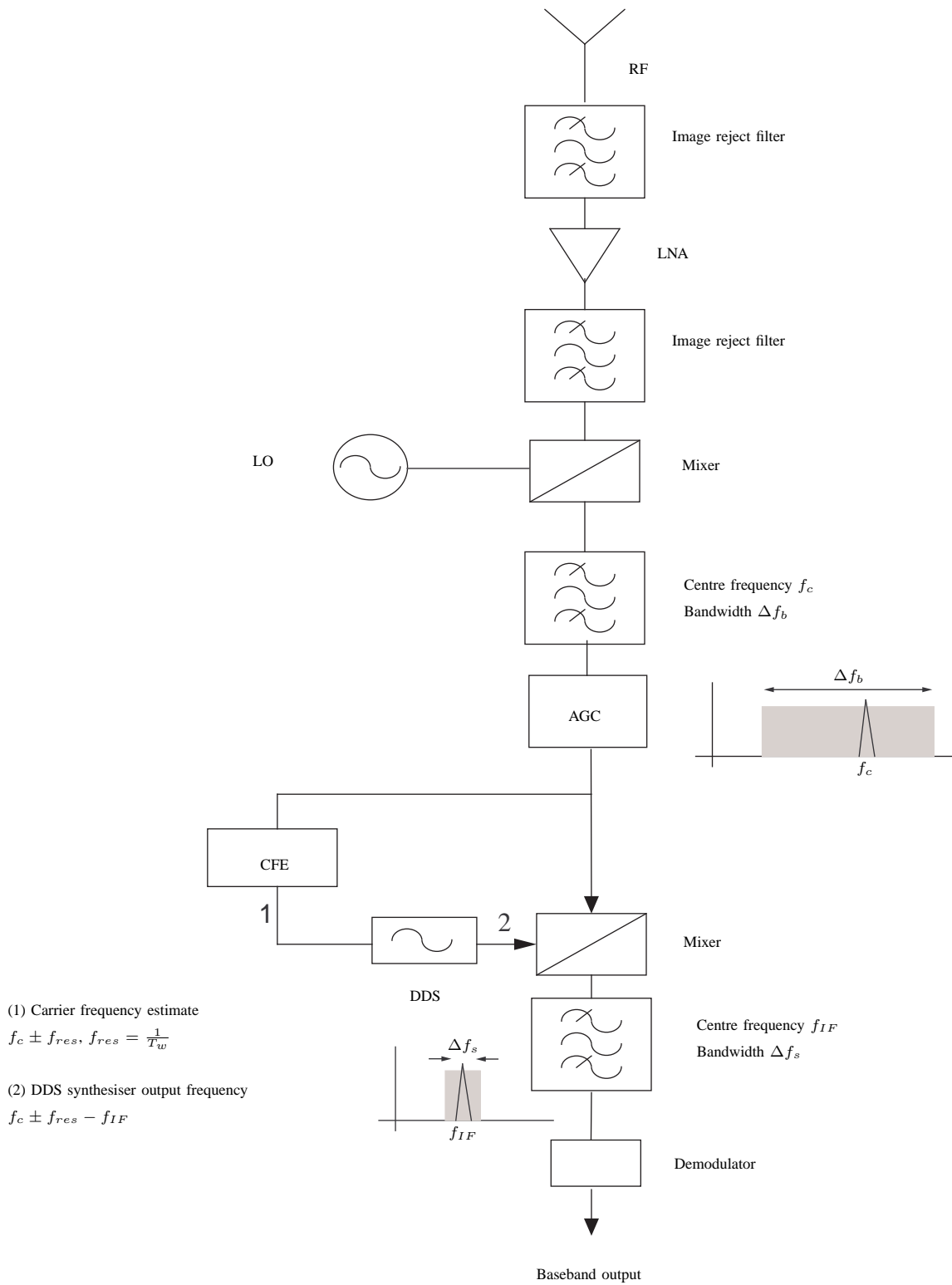


Figure 1. Tag reader receiver architecture

frequency must be resolved to a frequency resolution,  $f_{res}$ , of 125 kHz ( here a resolution of 1/8 of the data rate,  $R$ , has been chosen ). To accommodate this frequency resolution the pre-amble of the received signal must be measured for 8  $\mu$ s. The duration of the tag pre-amble,  $T_w$ , is usually set greater than 8  $\mu$ s to account for any latency encountered in the synchronisation procedure. A simple peak search algorithm is then able to detect the primary modulation components and distinguish them from even high-level noise or other interference, thus estimating its frequency to a precision of  $\pm 62.5$  kHz. The DDS is then set to the estimated frequency,  $f_c \pm f_{res}$  but with an offset equal to the desired final IF frequency,  $f_c \pm f_{res} - f_{IF}$  and then down-converts the signal to its final IF frequency,  $f_{IF}$ . Since the signal bandwidth,  $\Delta f_s$ , is around 1 MHz it is now an easy matter to demodulate by standard techniques, such as a Costas loop, which will acquire lock within a further couple of bit periods, well before the end of the pre-amble. For a  $\frac{c}{n_o}$  of  $2 \times 10^7$  (quite low), and an acceptable phase jitter of  $7^\circ$  rms, the loop natural frequency of the Costas loop should be 100 kHz. This should give fast tuning (around 2  $\mu$ s) of the Costas loop, provided the initial frequency offset is no more than around 200 kHz - say 2 FFT resolution cells [7].

For the 30 MHz detection bandwidth,  $\Delta f_b$ , considered in this design and an intermediate first stage frequency of 100 MHz, a 80 MHz bandpass sampler is sufficient in an FFT implementation of the carrier frequency estimator. The corresponding FFT size,  $N$ , can be calculated in the following manner. By rearranging (3) the FFT size is equal to  $\frac{T_w}{T_s}$ . Since the sample time,  $T_s$ , from the 80 MHz ADC is equal to 12.5 ns and  $T_w$  was calculated as 8  $\mu$ s, the FFT size,  $N$  is equal to 640 points. A high end dedicated DSP chip or an FPGA with a DSP core could perform an FFT of this size with a short latency of a few microseconds. The disadvantage of both approaches is the high purchase cost and additionally for the FPGA chip the development of a multilayer PCB board for the BGA chip interface. A viable alternative to an all digital CFE is an analog method that estimates the Fourier transform using surface acoustic wave (SAW) linear dispersive delay lines. This approach also remove the need for a 80 MHz ADC used in the digital implementations and the sliding Fourier transform estimate can be performed at a relatively high intermediate frequencies.

**A. Implementation of the carrier frequency estimator**

Chirp filters are commonly used in pulse compression radar systems. A second application of these devices is the compressive receiver which is a system for frequency measurement [8]. This system takes advantage of the linear dispersion delay with frequency property of the chirp filter in the measurement of the Fourier transform of the received signal. The chirp filters, which are also known as linear dispersive delay lines, have an impulse response with an instantaneous frequency that varies linearly as a function of time. The impulse response of the chirp filter

can be shown for a constant chirp rate,  $\mu(t)$ , as follows

$$g(t) = a(t) \cos(w_c t + \pi \mu t^2 + \phi_o) \tag{5}$$

where the chirp signal has length  $T_c$ , centre frequency  $w_c$  at time  $t = 0$  so that  $a(t) = 0$  for  $|t| > \frac{T_c}{2}$ , the envelope is flat so that  $a(t)$  is constant for  $|t| \leq \frac{T_c}{2}$  and  $\phi_o$  is a constant.

This response is utilised in the SAW chirp-Z-transform to form the power spectrum of the received signal,

$$F(2\pi\mu\tau^2) = e^{-j\pi\mu\tau^2} \int_{-\infty}^{+\infty} (x(t)e^{j\pi\mu t^2}) e^{j2\pi\mu(\tau-t)^2} \tag{6}$$

The process can be described as the multiplication of the input signal by a chirp waveform, followed by convolution with a chirp filter; the post multiplication with a third chirp waveform is used to correct the phase of the output waveform and is not needed if the power spectrum is desired. The power spectrum can therefore be found using a pair of chirp filters with opposing chirp directions. This method of frequency analysis is used quite widely in radio astronomy and microwave remote sensing [9], [10]. A schematic of the compressive receiver is shown in a M(long)-C(short) scheme in Figure 2. The impulse response of the expander is longer than the compressor, to ensure that the bandwidth of the signal can be completely compressed and provide an accurate spectrum estimate. As before the input signal  $x(t)$  is mixed with a linear downchirp waveform (expander) followed directly by a convolution in a linear upchirp filter (compressor). It can be shown that the output signal  $v(t)$  is a sliding Fourier transform [8].

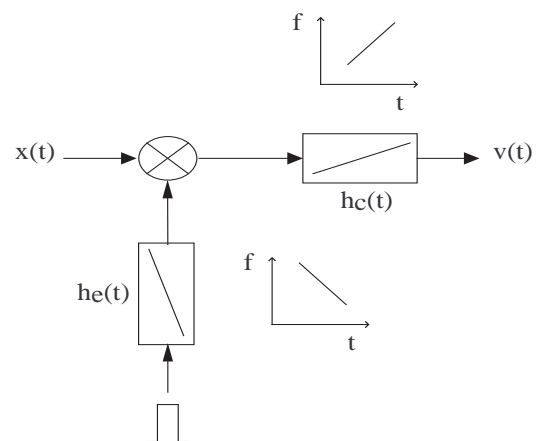


Figure 2. Schematic of the compressive receiver

The duty cycle is an important parameter when considering the compressive receiver as a frequency estimator because a carrier frequency estimate is required after each pre-amble duration,  $T_w$ , so that the DDS can be set to the correct frequency to allow the Costas loop to demodulate the data transmission. The repetition time of

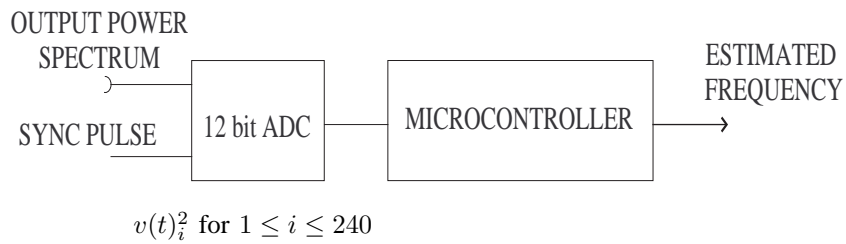
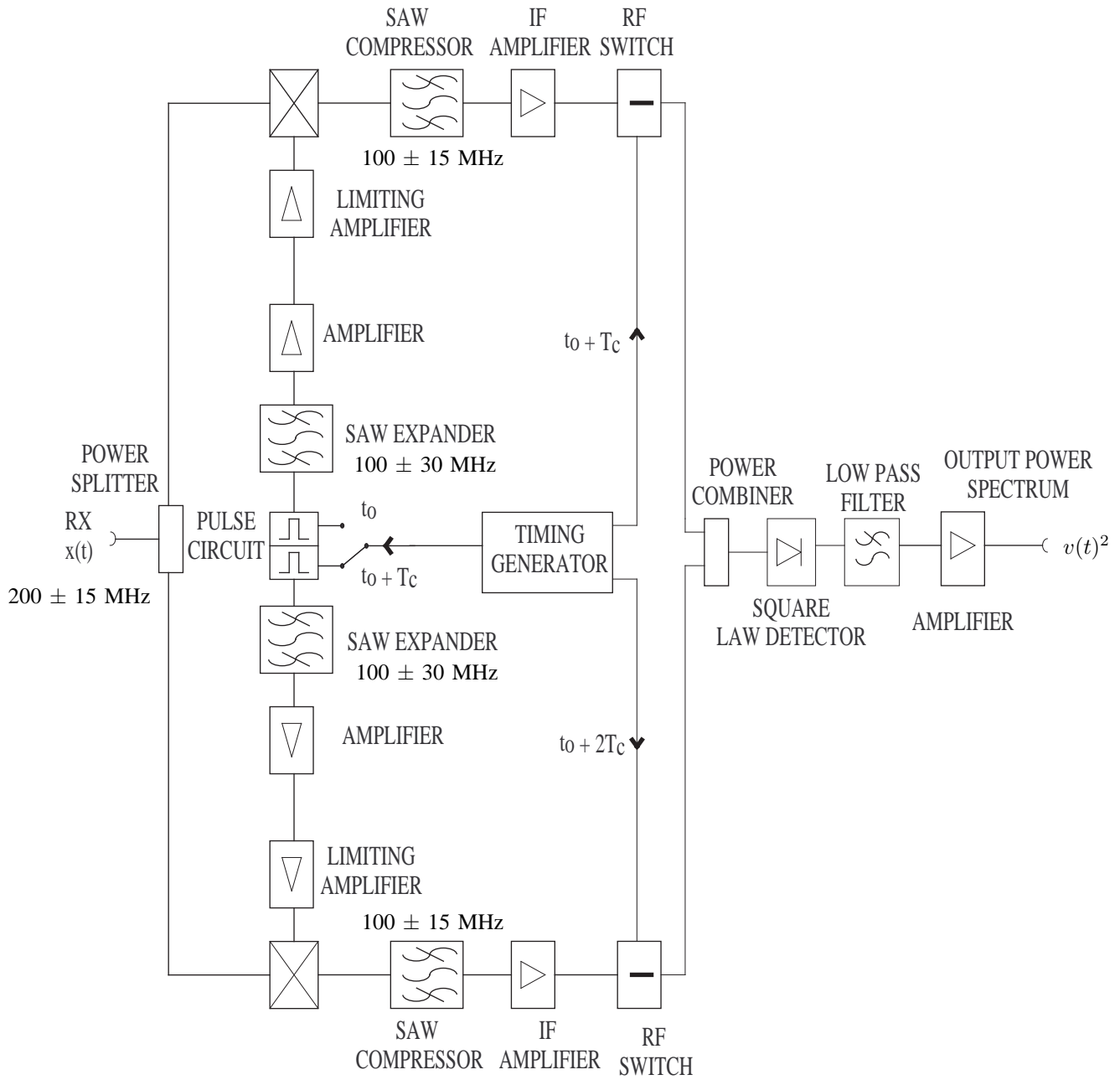


Figure 3. Architecture of the SAW carrier frequency estimator

the CFE module cannot be shorter than the compressor duration to avoid time-frequency ambiguity. One module will therefore only have a 50 % duty cycle and so two modules are required in push-pull mode to obtain a 100 % duty cycle as seen in the SAW CFE architecture shown in Figure 3. In this architecture, the input signal is passed to both Fourier transform modules operating in alternate fashion. The modules are switched at the appropriate times using the timing generator and RF switches. In each cycle the input signal is multiplied in a linear mixer with a linear expanding chirp waveform with a flat spectrum. This flatness is achieved with a saturating amplifier. On post multiplication the convolution is followed by suitable IF amplification. The power spectrum is assessed using a square law detector via additional low pass filtering and amplification. The output of the detector is sampled throughout the  $T_w$  period by an ADC and these samples are sent to a microcontroller. If there is sufficient time these samples could then be passed to an acquisition and integration circuit to improve the accuracy of the amplitude estimates.

The parameter bounds of the time dispersion,  $T_e$ ,  $T_c$ , and the bandwidth,  $B_e$ ,  $B_c$ , of the SAW chirp filters for the design are chosen to be well within those described by [11]. In general TB (time-bandwidth) products up to about 10,000 are possible. In this example, the compressor centre frequency is chosen as 100 MHz and a corresponding bandwidth,  $B_c$ , of 30 MHz. Working backwards, the expander must then mix down the RX signal to a band centred at the compressor centre frequency. In addition to ensure the frequency band of the compressor impulse response completely overlaps the signal band the expander bandwidth,  $B_e$ , must be chosen to be twice the compressor bandwidth,  $B_c$ , because the literature shows an optimum expander/compressor chirp length ratio of 2 to achieve a rectangular transform window [10], [11]. Assuming the input RX signal is chosen for convenience at a common IF of 200 MHz and has a bandwidth of  $\pm 15$  MHz then the expander centre frequency must therefore be chosen as 100 MHz with a bandwidth,  $B_e$ , of 60 MHz. The frequency resolution of the system is equal to the reciprocal of the length of the compressor impulse response,  $T_c$ . Hence for a desired frequency resolution,  $f_{res}$ , of 125 kHz (so as to be well within the Costas loop capture range),  $T_c$ , must be equal to  $8 \mu s$ . This is equivalent to 240 resolvable points – either by  $\frac{T_e B_e}{4}$  or alternately the compressor bandwidth  $B_c$  divided by the desired frequency resolution,  $f_{res}$ . Consequently if we retain the same chirp rate  $\mu$  for both chirp filters the expander impulse response,  $T_e$ , is equal to  $16 \mu s$ .

The dynamic range of the CFE will be reduced by not taking account of side lobe weighting to remove spectral leakage as a result of the finite Fourier transform estimation window,  $T_c$ . The performance for non-bin centre frequencies could be improved by as much as 0.82 dB using a Hamming window method. However at high SNR there should only be a small effect on the quality of the power spectrum estimate. An additional source of

error is manufacturing tolerances. Quartz material which is used to make the filters have a surface wave velocity which can be controlled to within 50 parts per million or better. At 100 MHz this is only 5 kHz error per tag transmission. This represents a negligible amount of error.

#### IV. ANALYSING THE PERFORMANCE OF THE CARRIER FREQUENCY ESTIMATOR

Before analysing the performance of the two peak search algorithms used in the carrier frequency estimator we model the received signal using the discrete FFT implementation in which the carrier signal is downconverted from a  $100 \pm 15$  MHz first IF band down to a  $20 \pm 15$  MHz frequency band as a result of undersampling by an ADC.

##### A. Received signal model

We begin the analysis of the estimator by showing that the baseband BPSK signal can be written as

$$S(t) = \sum_{n=-\infty}^{\infty} a_n p(t - T_b) \tag{7}$$

where:  $p(t)$  is the baseband NRZ pulse limited to  $T_b$  seconds and  $a_n$  is the pre-amble periodic sequence of alternating ones and minus ones representing binary ones and zeros.

Applying Fourier analysis to  $S(t)$  using an FFT of size,  $N$ , we find that frequency content in each FFT bin,  $S(k)$ , shown in Equation 8 is a weighted sum of the harmonics that have frequencies at odd multiples of  $\frac{1}{2T_b}$  Hz.

$$S(k) = \sum_{n=0}^{N-1} S(n) \exp\left(\frac{-j2\pi kn}{N}\right) = A \left( \frac{\sin\left(\frac{\pi(f-f_c)}{R}\right)}{\left(\frac{\pi(f-f_c)}{R}\right)} \right) \tag{8}$$

The amplitude and separation of the two largest spectral pairs are illustrated in Figure 4 whenever the BPSK binary modulation is superimposed on a carrier signal.

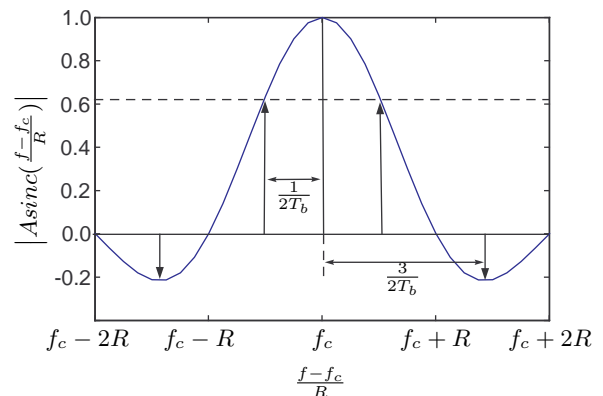


Figure 4. Theoretical spectra for a BPSK modulate carrier

Since the signal is located somewhere within the 5 - 35 MHz frequency band as a result of undersampling by

the ADC, the output of undersampling by the ADC can be modelled as

$$s(t) = Am(t) \cos 2\pi f_c t + \eta(t) \quad 0 \leq t \leq T_b \quad (9)$$

where:  $A$  is an amplitude constant,  $m(t) = +1$  or  $-1$ ,  $f_c$  is the unknown carrier frequency,  $T_b$  is the symbol duration of  $1 \mu s$ ,  $\eta(t)$  is a white Gaussian noise process with a mean of zero in a sampling bandwidth,  $\frac{f_{sb}}{2}$ , of 40 MHz.

The signal to noise power ratio of the signal received at the Costas loop can be set by appropriate voltage scaling of a white Gaussian noise process. The Gaussian white noise process has a probability density function that is uniformly distributed as illustrated in Figure 5.

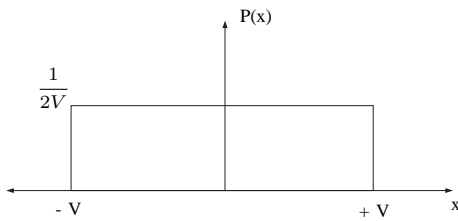


Figure 5. Probability density function of a white Gaussian noise process

The variance of the noise process can be given by

$$\begin{aligned} \sigma^2 &= \int_{-V}^{+V} x^2 P(x) \\ &= \frac{1}{2V} \left[ \frac{x^3}{3} \right]_{-V}^V \\ &= \frac{V^2}{3} \end{aligned} \quad (10)$$

The standard deviation,  $\sigma$ , of the noise process is therefore equal to

$$\sigma = \frac{V}{\sqrt{3}}$$

The scaling constant,  $V$ , is adjusted to set a desired noise spectral density,  $\eta_o$ , in the sampling bandwidth,  $\frac{f_{sb}}{2}$ . The noise spectral density in the sampling bandwidth can now be described as

$$\eta_o = \frac{V_{nsc}}{2\sqrt{3}} = \frac{V_{nsc}^2}{6f_{sb}} \text{ V}^2 \text{ Hz}^{-1} \quad (11)$$

rearranging the variables the scaling constant is found as

$$V_{nsc} = \sqrt{6f_{sb}\eta_o} \quad (12)$$

Since the noise power spectral density is set for a particular  $\frac{c}{\eta_o}$ , which is the carrier power to the noise power density ratio in units of dBHz at the input to the Costas loop demodulator, and the received carrier power  $c$  is set to  $1 \text{ V}^2$ , the noise spectral density can be found from  $c / (\frac{c}{\eta_o})$  and therefore the scaling constant  $V_{nsc}$  can be set in the model.

Having described a method of setting the rms noise level

in each FFT bin relative to a received carrier power,  $c$ , of  $1 \text{ V}^2$  we must then determine the absolute levels of the primary and secondary modulation spectral pair within the signal. First using (9) the amplitude,  $A$ , of the carrier is known to be equal to  $\sqrt{2c} = 1.41$ . The amplitude of the sidebands can then be calculated using (8), the first pair of sidebands have amplitude denoted  $0.636A$  and frequency separation  $\frac{1}{T_b}$  Hz; the second pair of sidebands have amplitude denoted  $0.212A$  and frequency separation  $\frac{3}{T_b}$  Hz.

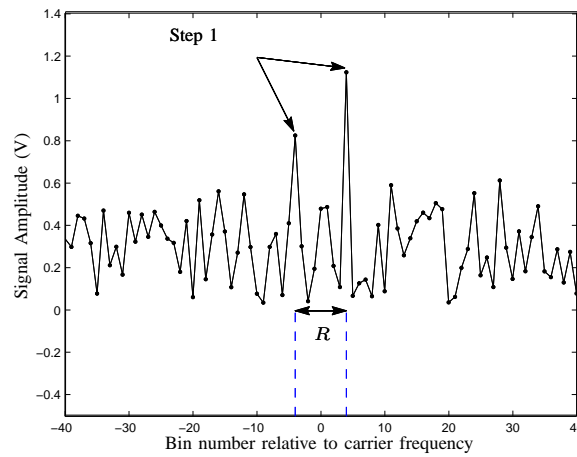
### B. Frequency estimation considerations

A number of factors must be evaluated before considering the accuracy of any potential peak search algorithm. The larger the number of cycles of data that is processed by the FFT then the greater is the likelihood of a successful peak search at low signal to noise power ratios. Since we can never have access to an infinite data record, a short time window must then be used to compute the FFT. This can lead to spectral leakage if the FFT is performed over a non-integer number of cycles of the input frequencies. This could lead to false detections by algorithms which use the two highest peaks as representing the primary spectral pair; for example if the two amplitudes reflect the same modulation position i.e. two samples on the same crest. Another problem occurs whenever the data window is not a power of two, in which case the FFT algorithm will append zeros to the data for the desired FFT window size and the frequency impulses in the spectrum will become a non-desirable sinc shaped. This can be explained by imagining the addition of  $d$  zeros is processed by the FFT in similar manner to taking a sinusoid and multiplying it with a rectangular box of length  $d$ . The multiplication of the box and a sinusoid in the time domain results in the convolution of a sinc with impulses in the frequency domain.

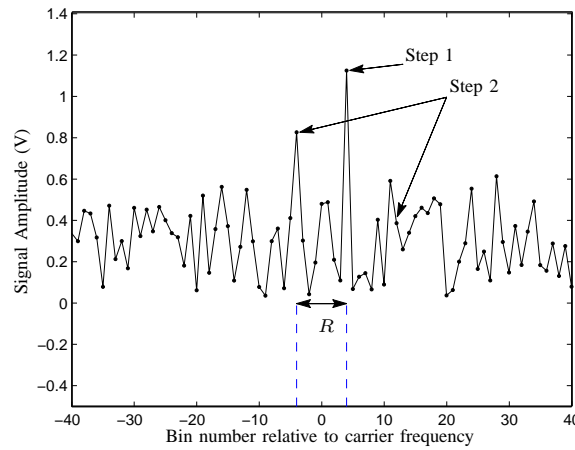
In light of the above discussion, the data is processed by the carrier frequency estimator in the following manner in order to obtain the best possible fit between the modeled and the simulated results for the peak search algorithms. First, the FFT window is maximized to obtain as high a resolution as possible considering technology, time constraints and the capture range of the demodulator. Second, the time window,  $T_w$ , is sampled with an FFT size,  $N$ , which is a power of 2. This results in no appended zeros and therefore no sidelobes due to 'sincing'. Third, the number of symbol cycles,  $N_{cycles}$ , which is calculated from  $\frac{T_w}{T_b}$ , is chosen to be an integer value so that there will be no spectral leakage. Provided the rules are followed the simulated and modeled results of the peak search algorithms discussed next should match consistently.

### C. Analysis of the peak search algorithms

The performance of the two peak search algorithms will be measured using the probability that the FFT search algorithm fails to estimate the carrier frequency with error no greater than the FFT resolution. The analysis of the algorithms will be based on the assumption that the received



(a) Algorithm I - (1) Pick the highest two peaks in the FFT



(b) Algorithm II - (1) Pick the highest peak in the FFT and then (2) Pick the highest peak in the FFT in a 2R Hz band centred on the index of the peak chosen in (1)

Figure 6. Illustration of the peak-search algorithms for a BPSK modulated carrier signal when  $\frac{c}{n_o} = 3 \times 10^6$

carrier frequency and the modulation components are separated by even multiples of the frequency resolution, i.e. on a bin centre. This is a first order approximation to a real situation where the carrier and its modulation components can be non-bin centred. In practise there is a fixed error associated with randomly received signal frequencies because they can be situated anywhere within the resolution bandwidth of  $\pm \frac{f_{res}}{2}$ . For instance if the carrier and its modulation components are located midway between bins, the magnitude of the FFT estimation at each of the bins drops to 0.64 of its maximum value and this reduces the probability of detection of the primary modulation components at low SNR.

*Algorithm I:* This algorithm which is illustrated in Figure 6(a) takes the average index value from the two indices  $k_{i=1,2}$  corresponding to the two largest peaks in the FFT of the received signal,  $S(k)$ , with the magnitude described as

$$P_k = |S(k)|, k = 0 \text{ to } N \quad (13)$$

and forms a frequency estimate  $\hat{f}_c$  of the carrier frequency  $f_c$ . It may be examined experimentally by simulation and also by analysis which extends the work of [2].

The output of the FFT for a signal containing modulation harmonics and noise can be modeled in the following manner. The magnitude  $P_k$  is a random variable whenever there are signals and noise present. In this analysis we neglect the condition of the signal frequency being half the sampling frequency for zero bias. The noise samples remain independent, normal and have zero mean with variance  $\sigma^2$ . Each non-tone bin can be shown to be a Rayleigh distribution denoted by a distribution  $C_n(P_k)$  and each tone bin has a Rician distribution ; for the first spectral pair it is denoted  $C_n(P_{r1})$  for tones with indices  $k = r1_a, r1_b$ , and for the second spectral pair it is denoted  $C_n(P_{r2})$  for tones with indices  $k = r2_a, r2_b$ . The other modulation components are neglected and are

modeled as non-tone bins.

$$C_{m1}(P_{r1}) = \frac{P_{r1}}{\sigma^2} \exp\left(\frac{-(P_{r1}^2 + b^2)}{2\sigma^2}\right) \cdot I_0\left(\frac{bP_{r1}}{\sigma^2}\right), \quad P_{r1} \geq 0 \quad (14)$$

$$C_{m2}(P_{r2}) = \frac{P_{r2}}{\sigma^2} \exp\left(\frac{-(P_{r2}^2 + c^2)}{2\sigma^2}\right) \cdot I_0\left(\frac{cP_{r2}}{\sigma^2}\right), \quad P_{r2} \geq 0 \quad (15)$$

$$C_n(P_k) = \frac{P_k}{\sigma^2} \exp\left(\frac{-P_k^2}{2\sigma^2}\right), \quad P_k \geq 0, \quad k \neq r1_a, r1_b, r2_a, r2_b \quad (16)$$

where:  $\sigma$  is the rms noise power in each FFT bin,  $b$  is the peak primary modulation amplitude, and  $c$  is the peak secondary modulation amplitude.

Having defined the probability distributions we can now develop the analytic probability of failure for algorithm I. The probability that one of the two primary tone indices  $r1_a$   $r1_b$  has the largest amplitude among all other bins is expressed as

$$P_s = [\Pr\{\text{all } C_n < C_{m1}\} \cap \Pr\{\text{both } C_{m2} < C_{m1}\}] \quad (17)$$

This be further expanded as

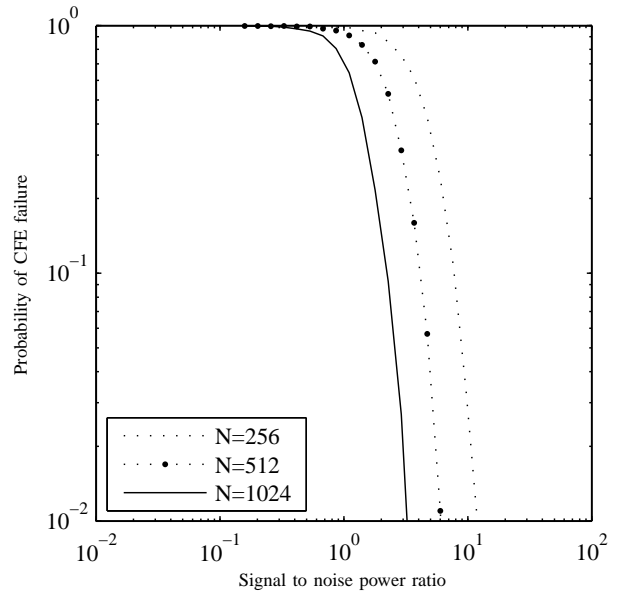
$$P_s = \int_0^x \Pr\{\text{all } C_n < C_{m1} | C_{m1} = x\} \cdot \left[ \int_0^x \Pr\{\text{both } C_{m2} < C_{m1} | C_{m1} = y\} dy \right] \cdot \Pr\{C_{m1} = x\} dx \quad (18)$$

This can be expanded by the multiplicative probability of the independent pdf distributions within each FFT bin. This is formed using the cdf of the Rayleigh distributions for the non-tone bins – that can be expressed analytically and the cdf of the Rician distributions for the second pair of spectral components – that can only be expressed numerically. Equation (19) shows the final evaluated function with substituted distributions pdf and cdf.

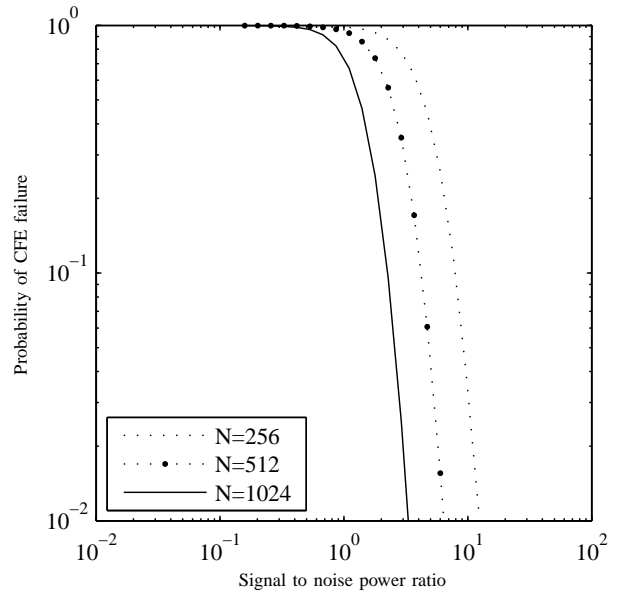
$$P_s = \int_0^\infty \left[ 1 - \exp\left(\frac{-x^2}{2\sigma^2}\right) \right]^{N-4} \cdot \left[ \int_0^x \frac{y}{\sigma^2} \exp\left(\frac{-(y^2 + c^2)}{2\sigma^2}\right) I_0\left(\frac{cy}{\sigma^2}\right) dy \right]^2 \cdot \left[ \frac{x}{\sigma^2} \exp\left(\frac{-(x^2 + b^2)}{2\sigma^2}\right) I_0\left(\frac{bx}{\sigma^2}\right) \right] dx \quad (19)$$

The probability of failure is the probability that two primary tone bins fail to be the highest two values. Since

both primary tone bins have probability distributions which are independent, the probability of both being the highest two values is  $P_s^2$ . Therefore the probability of FFT failure is  $P_{\text{failure}} = 1 - P_s^2$ . The accuracy of the analysis is demonstrated first for the probability of failure for a FFT of size 512 when compared to a monte carlo simulation with 3000 trials as shown in Figure 8(a). The accuracy of the model is repeatable for other FFT sizes as shown in Figures 7(a) and 7(b) which show that the modeled and simulated results for algorithm I closely match each other.



(a) Simulated probability of failure using algorithm I



(b) Analytic probability of FFT failure using algorithm I

Figure 7. Probability of FFT failure using algorithm I for FFT sizes of 256, 512 and 1024

*Algorithm II:* This algorithm which is illustrated in Figure 6(b) takes the largest spectral peak with index  $k_{i=1}$  and assumes it to be one of the primary tones. It then takes the second largest spectral peak with index,  $k_{i=2}$  from a 2R Hz bandwidth centred on the index of the first spectral peak and then assumes this to be the second primary tone. The algorithm is successful provided the first spectral peak happens to coincide with one of the primary tone indices and the other primary tone has the highest amplitude in a bandwidth 2R centred on the index of the first spectral peak. The analysis of the algorithm can be approximated by the following method. The probability of FFT success is the probability that one of the two primary tone indices  $r1_a$  and  $r1_b$  happens to have the largest amplitude among all other bins and the other tone bin happens to have highest amplitude among all other bins in a 2R Hz band surrounding the first located tone bin. The analysis of probability then proceeds in a similar manner to Algorithm I. First, the probability that the largest peak has an index equal to one of the primary modulation pair is  $P_{s1}$ . This will occur if one the primary tone bins happens to be the highest among all other bins.

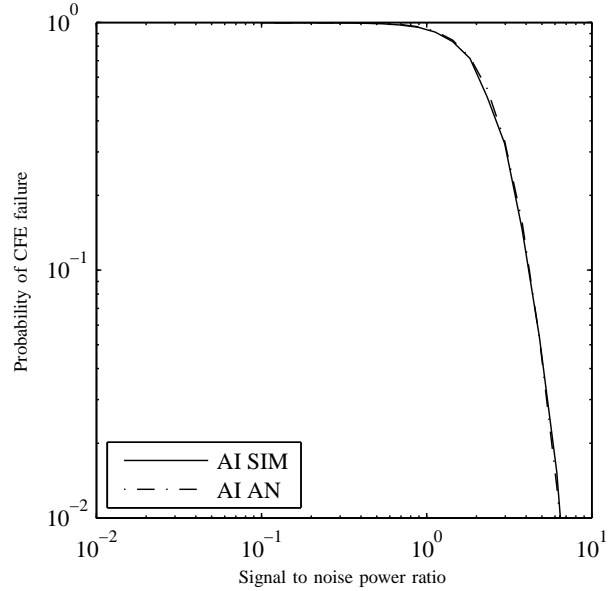
$$\begin{aligned}
 P_{s1} = & \int_0^\infty \left[ 1 - \exp\left(\frac{-x^2}{2\sigma^2}\right) \right]^{N-4} \\
 & \cdot \left[ \int_0^x \frac{z}{\sigma^2} \exp\left(\frac{-(y^2 + b^2)}{2\sigma^2}\right) I_0\left(\frac{by}{\sigma^2}\right) dz \right] \\
 & \cdot \left[ \int_0^x \frac{y}{\sigma^2} \exp\left(\frac{-(y^2 + c^2)}{2\sigma^2}\right) I_0\left(\frac{cy}{\sigma^2}\right) dy \right]^2 \\
 & \cdot \left[ \frac{x}{\sigma^2} \exp\left(\frac{-(x^2 + b^2)}{2\sigma^2}\right) I_0\left(\frac{bx}{\sigma^2}\right) \right] dx
 \end{aligned} \tag{20}$$

The probability that the second primary tone is highest in a 2R Hz band centred on the first tone is  $P_{s2}$ .

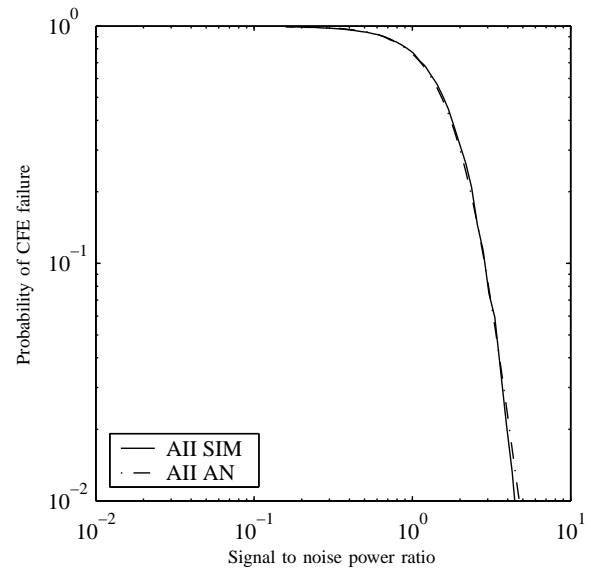
$$\begin{aligned}
 P_{s2} = & \int_0^\infty \left[ 1 - \exp\left(\frac{-x^2}{2\sigma^2}\right) \right]^{2R-3} \\
 & \cdot \left[ \int_0^x \frac{y}{\sigma^2} \exp\left(\frac{-(y^2 + c^2)}{2\sigma^2}\right) I_0\left(\frac{cy}{\sigma^2}\right) dy \right] \\
 & \cdot \left[ \frac{x}{\sigma^2} \exp\left(\frac{-(x^2 + b^2)}{2\sigma^2}\right) I_0\left(\frac{bx}{\sigma^2}\right) \right] dx
 \end{aligned} \tag{21}$$

The probability of an FFT success is equal to the probability of index combinations  $(r1_a, r1_b)$  and  $(r1_b, r1_a)$ . The probability of FFT failure is therefore equal to  $P_{failure} = 1 - 2P_{s1}P_{s2}$ . The accuracy of the analysis is demonstrated first for the probability of failure for an FFT of length 512 when compared to a monte carlo simulation with 3000 trials as shown in Figure 8(b). The performance of algorithm II can then be compared with algorithm I as seen in the results in Figures 9(a) and 9(b) for  $N = 512$ .

The results indicate that, as expected, Algorithm II has superior performance to Algorithm I at low signal to noise ratios. Both methods determine the carrier frequency with a low probability of error above 10 dB SNR in 1 MHz signal bandwidth for an FFT of length 512.

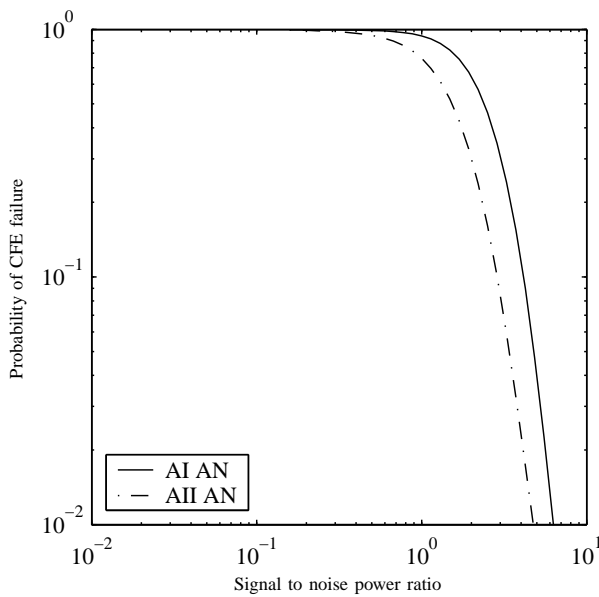


(a) Simulated and analytic probability of failure using Algorithm I

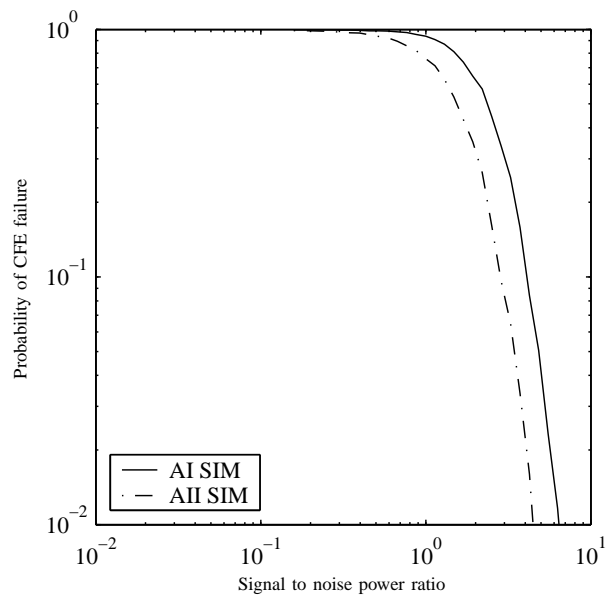


(b) Simulated and analytic probability of failure using algorithm II

Figure 8. Simulated and analytic probability of failure using algorithms I and II for an FFT of size 512



(a) A comparison of the analytic probability of failure for algorithms I and II for an FFT



(b) A comparison of the simulated probability of failure for algorithms I and II

Figure 9. A comparison of the probability of failure for algorithms I and II for an FFT size of 512

It should be noted that algorithm I provides a simpler implementation when used in the architecture shown in Figure 3 because it computes the frequency estimate in less steps than algorithm II. In fact Algorithm I could be implemented in the microcontroller by continuously updating the address pointers to the indices with the largest and second largest magnitudes every time a sample enters the microcontroller. This can be easily achieved as long the speed of the processor is faster than the delay between samples entering the microcontroller. Significantly, the estimation of the carrier frequency would take no more than a couple of  $\mu\text{s}$  after the last sample of the power spectrum has entered the processor. The DDS can then be set to the correct frequency before the end of the pre-amble duration,  $t_w$ , to allow the Costas loop to demodulate the data transmission.

A slower, complicated but yet more accurate approach can be implemented using algorithm II. Algorithm II requires that the second peak chosen must be the largest in a  $2R$  Hz band centred on the index of the largest peak chosen from step one. This implies that the samples in this band must be ordered into descending numerical order. The sorting of these samples is not trivial and can only be performed after the last sample has entered the microcontroller. The number of operations for the simplest slowest sorting algorithms have  $O(n^2)$  and the fastest algorithms have  $O(n \log n)$ . Whilst a discussion of these algorithms is beyond the scope of this work, let's consider a slow sorting algorithm operating on the samples in the band using a 16 MHz ATmega microcontroller. The number of samples in the band is dependent on the data rate and frequency resolution, if the data rate,  $R$ , is 1 MHz and  $f_{res}$  is 125 kHz, then the number of samples in the band

is 16. Applying an algorithm complexity of  $O(n^2)$  to sort these samples would take approximately  $16 \mu\text{s}$ . This is in addition to the time of  $8 \mu\text{s}$  taken to analyse the signal during the pre-amble duration,  $t_w$ , as well as any other latency caused by the settling times of the DDS and Costas loop used in the receiver design.

A much longer tag pre-amble duration must be accommodated when using algorithm II in the carrier frequency estimator. The length of the pre-amble duration could be reduced by operating algorithm II using a faster processor which causes additional cost or reducing the frequency resolution which causes a higher probability that the algorithms would fail at low SNR. Moreover increasing the pre-amble length implies that the data burst will be much longer and thus the number of the RF-ID tags that can be accommodated reliably for a given mean update time will also be lower. These factors must be considered carefully before the implementation of algorithm II in the carrier frequency estimator.

## V. CONCLUSIONS

A novel RF-ID receiver architecture incorporating frequency diversity was presented. The architecture allows RF-ID tags with oscillators of low frequency stability to be accommodated within the same RFID cell. In the prototype design, the RFID tags can transmit at carrier frequencies anywhere within a wide band of 30 MHz centred on 5.8 GHz but in principle an arbitrarily-wide band can be accommodated. The synchronisation technique used by the receiver has a carrier frequency estimator which is implemented here with SAW dispersive delay chirp filters as an alternative to a conventional FPGA or DSP implementation. The synchronisation technique contained

in the receiver uses the spectral properties of a short preamble at the beginning of the received pulse to estimate the carrier frequency and then immediately directs a DDS-based LO to the appropriate frequency. The performance of the carrier frequency estimator has been examined using two peak search algorithms. The results indicate that Algorithm II has superior performance to Algorithm I at low signal to noise ratios, although the implementation of Algorithm I leads to lower latency in the estimation of the carrier frequency because algorithm II uses an additional unavoidable step involving the sequencing of the data samples.

The validity of the architecture presented in the paper has been established using analytical models and monte carlo simulation of the carrier frequency estimator but could be enhanced further using a more detailed behavioral model of the proposed design that includes the desired specifications of latency, frequency resolution and reliability. The use of wide band synchronisation in an active RF-ID system provides a considerable improvement in the robustness of the active RF-ID system to frequency interference from other systems but equally important this approach also allows for a highly-gearred trade-off between extra reader cost and consequential tag savings.

#### ACKNOWLEDGMENT

The authors gratefully acknowledge the support of EU project officer Jean-Pierre Lentz throughout the three year period of the OPTAG project.

#### REFERENCES

- [1] A. D. Whalen, *Detection of Signals in Noise*. New York: Academic Press, 1971.
- [2] D. C. Rife and R. R. Boorstyn, "Single-tone parameter estimation from discrete-time observations." *IEEE Transactions on Information Theory*, vol. IT-20, no. 5, pp. 591 – 598, 1974.
- [3] —, "Multiple tone parameter estimation from discrete-time observations." *Bell System Technical Journal*, vol. 55, no. 9, pp. 1389 – 1410, 1976.
- [4] S. Holm, "Optimum fft-based frequency acquisition with application to cospas-sarsat," *IEEE Trans. Aerosp. Electron. Syst. (USA)*, vol. 29, no. 2, pp. 464 – 75, 1993.
- [5] W. K. Ahmed and P. J. McLane, "Method for coarse frequency acquisition for nyquist filtered mpsk," *IEEE Transactions on Vehicular Technology*, vol. 45, no. 4, pp. 720 – 731, 1996.
- [6] M. Nezami, R. Sudhakar, and H. Helmken, "Dft-based frequency acquisition algorithm for large carrier offsets in mobile satellite receivers," *Electron. Lett. (UK)*, vol. 37, no. 6, pp. 386 – 7, 2001.
- [7] P. V. Brennan, *Phase-Locked Loops: Principles and practice*. McGraw-Hill, 1996.
- [8] D. P. Morgan, *Surface-Wave Devices for Signal Processing*. Elsevier, 1985.
- [9] Y. Zhang, J. Gong, X. Zhou, Y. Wei, and J. Cheeke, "High-resolution spectrometer systems based on saw chirp filters," *1997 IEEE Ultrasonics Symposium Proceedings. An International Symposium (Cat. No.97CH36118)*, vol. 1, pp. 89 – 92, 1997.
- [10] P. Hartogh and G. Hartmann, "A high-resolution chirp transform spectrometer for microwave measurements," *Meas. Sci. Technol. (UK)*, vol. 1, no. 7, pp. 592 – 5, 1990.
- [11] M. A. Jack, P. M. Grant, and J. H. Collins, "Theory, design, and applications of surface acoustic wave fourier-transform processors." *Proceedings of the IEEE*, vol. 68, no. 4, pp. 450 – 468, 1980.

**Thomas M. McCoy** graduated with a first class MEng degree in Electrical and Electronic engineering from Queen's University Belfast, Northern Ireland, in 2002. He has previously achieved sponsored placements at Celeritek UK Ltd and worked as a researcher associate with Anglia Ruskin University.

He is currently a Ph.D. candidate at UCL, London, UK. His research interests include RF-ID, communication system design and phase locked loops.

**Paul V. Brennan** was born in London, UK in 1963 and obtained a BSc(Eng) degree in 1984 and a PhD degree in 1988 in electronic & electrical engineering from University College London. After a short spell working on frequency-agile transceivers for Plessey Military Communications he rejoined University College London as a Research Fellow and is now a Professor in microwave electronics. He has published widely in many areas including RF and microwave electronics, antennas, radar and phase-locked loops, including a textbook 'Phase-locked loops. Principles and practice' (McGraw Hill/Macmillan, 1996) on the subject. His current research interests include phase-locked loop frequency synthesis, RF-ID tag location and phased array antennas. Prof Brennan is a Fellow of the Institute of Engineering and Technology.

**Richard J. Bullock** is a research associate in the department of Electronic and Electrical Engineering at University College London and works for Paul Brennan. His research interests include radar signal processing and aircraft-borne interferometric SAR.